

# Rank-One Prior: Real-Time Scene Recovery

Jun Liu, Ryan Wen Liu, Jianing Sun, Tieyong Zeng

**Abstract**—Scene recovery is a fundamental imaging task with several practical applications, including video surveillance and autonomous vehicles, etc. In this paper, we provide a new real-time scene recovery framework to restore degraded images under different weather/imaging conditions, such as underwater, sand dust and haze. A degraded image can actually be seen as a superimposition of a clear image with the same color imaging environment (underwater, sand or haze, etc.). Mathematically, we can introduce a rank-one matrix to characterize this phenomenon, i.e., rank-one prior (ROP). Using the prior, a direct method with the complexity  $O(N)$  is derived for real-time recovery. For general cases, we develop ROP<sup>+</sup> to further improve the recovery performance. Comprehensive experiments of the scene recovery illustrate that our method outperforms competitively several state-of-the-art imaging methods in terms of efficiency and robustness.

**Index Terms**—Rank-one prior, underwater, sand dust, haze, unified spectrum.

## 1 INTRODUCTION

A  $\text{N}$  image is worth a thousand words. However, an image or a video captured in a turbid medium provides insufficient and incorrect visual information. For instance, Fig. 1 shows five images captured in different turbid media, such as sand dust, underwater, and haze. These images suffering from severe contrast and color alteration or degradation increases the difficulty in many important computer vision tasks, including image classification [1], object detection [2], surveillance systems [3], and semantic segmentation [4]. Hence, correct scene recovery from degraded observation is an essential and fundamental step in computer vision.

Generally, the degradation of underwater, sand dust and hazy images is due to light absorption and scattering [5], [6], [7], [8], [9]. More specifically, 1) due to the physical properties of the environmental medium, visible light is scattered. Therefore, the ambient light source will consist of original visible light and scattered light; 2) usually, the imaging device completes the imaging process by capturing light emission from the object scene. Since the environmental medium absorbs visible light, the acquired radiation intensity is attenuated. Moreover, the degree of attenuation depends on the distance between the object and the imaging device. Many important scene recovery problems, such as sand dust/underwater image enhancement and image dehazing, are handled as different computer vision tasks. However, from an imaging point of view, these problems have common characteristics: color distortion, low contrast, and low visibility.

- J. Liu is with the Key Laboratory of Applied Statistics of MOE/School of Mathematics and Statistics, Changchun, Jilin, 130024, China.  
E-mail: liuj292@nenu.edu.cn
- W. Liu is with Department of Mathematics, School of Navigation, Wuhan University of Technology, China  
E-mail: wenliu@whut.edu.cn
- J. Sun is with School of Mathematics and Statistics, Northeast Normal University, Changchun, Jilin, 130024, China. Corresponding author.  
E-mail: sunjn118@nenu.edu.cn
- T. Zeng is with Department of Mathematics, The Chinese University of Hong Kong, Shatin, NT, Hong Kong  
E-mail: zeng@math.cuhk.edu.hk

Suppose that  $\mathbf{I} \in \mathbb{R}^{m \times n \times 3}$  is the observed degraded image,  $\mathbf{J} \in \mathbb{R}^{m \times n \times 3}$  is the clear image. The widely used physical model describing the formation of an image suffering from light transmission hazard [10], [11] is defined as follows:

$$\mathbf{I}(x) = t(x) \circ \mathbf{J}(x) + \tilde{t}(x) \circ \mathbf{A}, \quad (1)$$

where the pixel coordinate  $x \in \Omega$  and  $\Omega$  is the domain of the pixel location. Notably,  $\Omega$  has  $mn$  elements,  $\circ$  is the component-wise multiplication,  $\mathbf{A} \in \mathbb{R}^{1 \times 1 \times 3}$  is the global ambient light<sup>a</sup>,  $t \in \mathbb{R}^{m \times n \times 3}$  is the medium transmission describing the portion of light reaching the camera, and  $\tilde{t}$  is the scattering map describing the portion of the scattered light that influences imaging. Moreover,  $\tilde{t}(x) + t(x) = (1, 1, 1)$ . To recover the clear image  $\mathbf{J}$ , the transmission  $t$  (or equivalently, the scattering map  $\tilde{t}$ ) and the ambient light  $\mathbf{A}$  are required. This task is challenging since both variables are unknown. The problem is considered under-determined since we usually have only one degraded image.

Note that in the homogeneous medium, the transmission  $t(x)$  in Eq. (1) can be expressed as follows:

$$t(x) = e^{-\beta d(x)}, \quad (2)$$

where  $\beta$  is the attenuation coefficient of the environment medium and  $d(x)$  is the scene depth. Generally,  $\beta$  is wavelength-dependent [12], [13] and hence  $t$  can differ per color channel.

Previous studies show that scene recovery has received extensive attention, with rich and outstanding results, and the related research is still progressing. The scene recovery methods can be divided into two main categories: traditional physical model methods (e.g., DCP [5]) and data-driven-based methods (e.g., end-to-end learning methods). This paper focuses on the first category due to its simplicity, stability, and flexibility. In our preliminary work [14], we proposed a straightforward and unsupervised method for estimating the transmission. This practical and efficient

a. For simplicity, we regard  $\mathbf{A} \in \mathbb{R}^{1 \times 1 \times 3}$  as  $\mathbf{A}^{1 \times 3}$ .

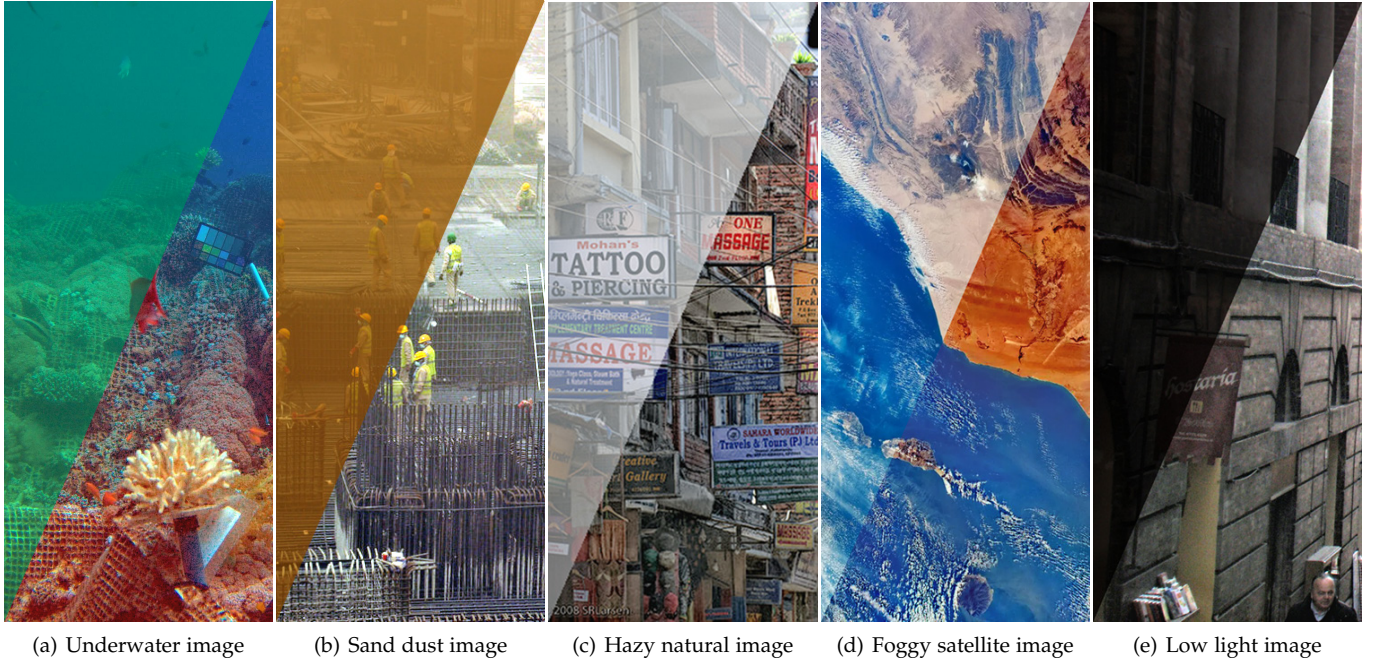


Fig. 1: Example of the scene recovery in different imaging conditions. The upper triangles in (a)-(e) are degraded patterns and the corresponding restored patterns by our method are shown in the lower triangles.

method performs well for various applications under different weather/imaging conditions. The complexity of transmission estimation is  $O(N)$ , where  $N$  is the single image's size. Compared with our preliminary work [14], we have made the following considerable improvement in this work:

- We give a detailed analysis and discussion on rank one prior for scene recovery;
- We propose a new  $\text{ROP}^+$  method to improve the accuracy of the scattering map.
- We evaluate the performance of  $\text{ROP}$  and  $\text{ROP}^+$  by using two well-known non-reference indexes NIQE (Natural Image Quality Evaluator [15]) and PIQE (Perception-based Image Quality Evaluator [16]) on the collected dataset including Real Underwater, Sand dust, and Hazy images (RUSH).
- We add more experimental results, including the new purple haze removal and low-illuminated image enhancement. We also provide interesting potential applications in supplemental materials, including snowy color correction, starry sky recovery, image quality improvement of photos taken from the projection screen, airplane window image enhancement, and bad weather image enhancement and segmentation.

## 2 RELATED WORK

Clear scene meets human visual needs and benefits for higher-level processing. In this section, we briefly highlight some related works in different imaging conditions.

**Image dehazing:** Narasimhan and Nayar [18] derived geometric constraints on scene color changes and developed algorithms for recovering scene colors upon appearing

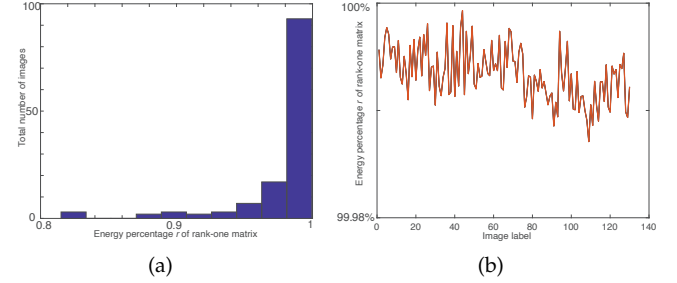


Fig. 2: Energy percentage of the obtained rank-one approximations. (a) Transmission map is computed using the physical image formation model. (b) Transmission map is computed using an existing transmission estimation method [17].

on a clear day. Furthermore, they presented a physics-based model describing scene appearances in uniform bad weather and proposed a fast algorithm to restore scene contrast [19]. From the assumption that transmission and surface shading are locally uncorrelated, Fattal [20] estimated the surface albedo and inferred the medium transmission. Tan [21] proposed to remove haze by maximizing the local contrast of the restored image. Their proposed method is based on observations that haze-free images have more contrast than images plagued by bad weather, and the air light is smooth. Fang et al. [22] proposed to handle the hazy image in the YUV color space using two priors. They showed that most of the chrominance information of an image could be well preserved. He et al. [5] proposed the well-known dark channel prior (DCP) using the statistical difference between haze-free and clear images. Afterward, numerous DCP-based methods [17], [23], [24], [25], [26] were

proposed. Golts et al. [26] proposed a dehazing method for the unsupervised training of deep neural networks using DCP loss. Unlike DCP, which assumed zero minimal value in local patches, Fattal [27] proposed a single image dehazing method using the color-lines pixel regularity in natural images. There were also some other effective priors, to name a few, color attenuation prior [28], non-local prior [29], color ellipsoid prior [30], gradient channel prior [31], and gamma correction prior [32], etc.

Recently, convolutional neural network (CNN)-based dehazing methods have gained tremendous attention in single-image restoration. For example, Cai et al. [33] proposed a DNN (DehazeNet) for the transmission map and used the conventional method to estimate atmospheric light. Furthermore, a multiscale version of Dehazenet [34] was trained to estimate the transmission map. Li et al. [35] proposed directly restoring the latent sharp image from a hazy image using a lightweight CNN (AOD-Net). Yang and Sun [36] offered a proximal Dehaze-Net by incorporating the haze imaging model, dark channel, and transmission priors in a deep architecture. Wu et al. [37] developed an autoencoder-like contrastive regularization (AECR)-Net for single image dehazing, consisting of autoencoder-like (AE) and contrastive regularization (CR) networks. Additionally, the generative adversarial network (GAN), an unsupervised learning method, has been used to achieve significant success in scene recovery [38], [39], [40].

**Underwater image enhancement:** Due to absorption, scattering, and attenuation of the reflected light from the underwater scene, underwater images have poor visual features, such as low contrast and color shift. Ancuti et al. [41] developed a fusion-based method using the input and corresponding weight maps. A similar but further exploration of image fusion was studied in [42]. Due to some similarities between hazy and underwater image modeling, some DCP-based methods were proposed [43], [44], [45]. Fu et al. [46] proposed a retinex-based enhancing method for a single underwater image. Furthermore, they proposed a simple yet effective two-step enhancing strategy, i.e., color correction and contrast improvement in the first and second steps, respectively [47]. Chiang and Chen [48] proposed a wavelength compensation and image dehazing (WCID) algorithm to handle light scattering and color change distortions. Inspired by the morphology and function of the teleost fish retina, Gao et al. [49] proposed an effective underwater image enhancement model. Berman et al. [50] used the haze-lines model for underwater image enhancement and constructed a new quantitative dataset. Jamadandi and Mudenagudi [51] proposed a deep learning framework to enhance underwater images using wavelet-corrected transformations. Li et al. [52] constructed an underwater image enhancement benchmark and proposed an underwater image enhancement network (Water-Net). Furthermore, Li et al. [9] adopted the CNN network to perform underwater image enhancement by assuming the underwater scene prior. Liu et al. [40] proposed a deep multiscale feature fusion net using the conditional generative adversarial network for underwater image color correction. Guo et al. [53] proposed a new multiscale dense generative adversarial network for enhancing underwater images. Li and Zhuang [54] proposed a fusion adversarial network for

enhancing real underwater images (Dewater-Net). Recently, Anwar and Li [55] gave a survey on underwater image enhancement using deep learning-based methods. For real-world underwater image enhancement (RUIE), Liu et al. [56] set up an undersea image capturing system and constructed a large-scale data set.

**Sand dust image enhancement:** Compared with studies on image dehazing and underwater image enhancement, there are few studies on sand dust image enhancement. Fu et al. [8] proposed a sand dust image enhancement approach using fusion principles. Wang et al. [57] proposed to convert the sand dust images into CIELAB color space and enhance the illuminant component by filtering. Peng et al. [11] proposed a generalized dark channel prior (DCP) approach for single image restoration, including sand dust image enhancement. Yang et al. [58] first transformed the sand-dust image into a hazy image by histogram matching and then applied Gaussian adaptive transmission to dehaze it. Since the blue channel information in sand-dust images is severely lost, Cheng et al. [59] considered compensating the blue channel and applying guided image filtering to enhance the image contrast and edge accuracy. Also, Wang et al. [60] proposed a fast color balance and multi-path fusion method for sand dust image enhancement. Their approach considered compensating for the blue channel attenuation. Gao et al. [61] considered handling degraded images in YUV color space. Si et al. [62] recently constructed a Sand-dust Image Reconstruction Benchmark (SIRB) for training Convolutional Neural Networks (CNNs) and evaluating algorithms performance. Due to the lack of real sand dust images for neural network training, such synthetic datasets will promote related research in the future.

**Low-light image enhancement:** From a statistical point of view, the inverted low-light images and hazy images have similar characteristics. Therefore, the DCP-based methods [63], [64] have been successfully exploited to improve the brightness of low-light images. However, the reversed low-light and hazy images still have noticeable differences, resulting in unnatural color performance in the local areas of enhanced image. Pizer et al. [65] proposed a histogram equalization (HE) method, which achieves image enhancement by flattening the distribution of pixel intensities or colors. The Retinex theory [66], and Retinex-based methods [67], [68] decompose the low-light image into reflection and illumination components, thereby can improve brightness while retaining the image details by estimating the reflection and illumination. However, traditional methods are challenging to extract the enhanced details effectively and are accompanied by phenomena such as low contrast and unnatural colors. The learning-based methods have made incredible breakthroughs in low-light image enhancement. The zero-reference learning method [69] can generate high-quality enhanced images with low computational cost. Wang et al. [70] proposed to embed a new normalization model into the enhancement network, which significantly improves the network's ability to retain background structural features and noise removal. In [71], Liu et al. presented a systematic review and evaluation of existing single-image low-light enhancement algorithms.

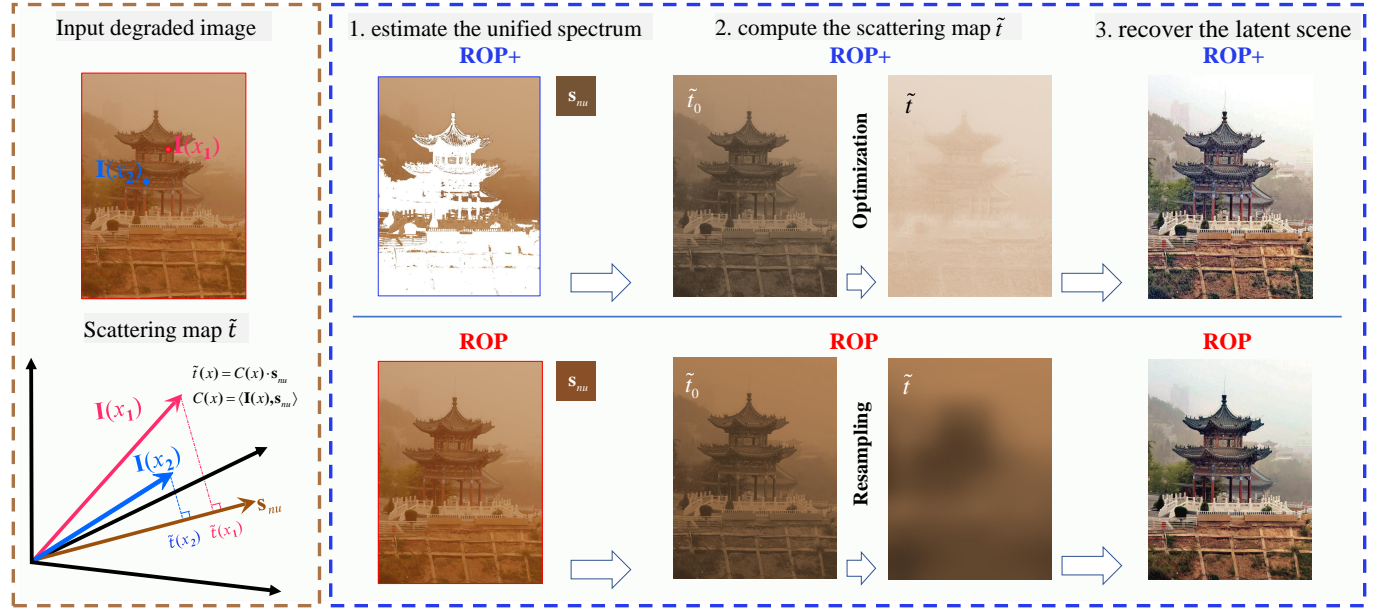


Fig. 3: Flowchart of the proposed methods.  $s_{nu}$  denotes the corresponding unified spectrum. The projection of  $I(x)$  onto the unified spectrum is the initial scattering map  $\tilde{t}_0(x)$ . In ROP<sup>+</sup>, the white regions are excluded for estimating  $s_{nu}$ .

### 3 RANK-ONE PRIOR

#### 3.1 Heuristics representation

For outdoor degraded images, we assume that most imaging scene areas covered by the ambient light are spatially homogenous except for the global ambient light. The scattering map  $\tilde{t}$  depends on the thickness of the scattered medium. Since the spectrum of the scattered light is a crucial feature of the imaging medium, the scattering map is highly related to the spectrum. For simplicity, the normalized spectrum is referred to as the unified spectrum. More specifically, we describe the relationship between the scattering map and the spectrum using a linear correlation given by

$$\tilde{t}(x) = C(x) \cdot \mathbf{b}, \quad (3)$$

where  $C \in \mathbb{R}^{m \times n}$ ,  $C(x) \in \mathbb{R}$  and  $x$  is the pixel coordinate. Here, we call  $C(x)$  the scattering coefficient and  $\mathbf{b} \in \mathbb{R}^{1 \times 3}$  the basis of  $\tilde{t}$ . The scattering map  $\tilde{t} \in \mathbb{R}^{m \times n \times 3}$  is a third-order tensor. The mode-3 unfolding of  $\tilde{t}$  is a matrix  $\tilde{T} \in \mathbb{R}^{3 \times mn}$ . It is not difficult to check that

$$\tilde{T} = (\mathbf{c}\mathbf{b})^\top, \quad (4)$$

where  $\mathbf{c}$  is the column-major vectorization of  $C$ . Apparently,  $\tilde{T}$  is a rank-one matrix. This is *rank-one prior* (ROP) on the scattering map  $\tilde{t}$ . In subsection 3.2, we verify its reasonableness using a statistical experiment on the transmission map  $t$ . Note that  $t(x) + \tilde{t}(x) = (1, 1, 1), \forall x \in \Omega$ .

#### 3.2 Statistical validation

In this subsection, we provide statistical support for the correctness of our rank-one prior. We conduct statistical experiments on several novel datasets, including I-Haze [72], O-Haze [73], and Dense-Haze [74], respectively. These datasets contain real hazy images obtained in indoor and outdoor environments. I-Haze and O-Haze were employed

in the dehazing challenge of the NTIRE 2018 CVPR workshop [75]. Dense-Haze was used in the dehazing challenge of the NTIRE 2019 CVPR workshop [76]. Unlike other dehazing databases, hazy images in I-Haze, O-Haze, and Dense-Haze were generated using real haze produced by a professional haze machine. We collected 30 pairs of real hazy and corresponding haze-free images of various indoor scenes from I-Haze, 45 pairs of outdoor scenes from O-Haze, and 55 pairs of dense homogeneous hazy and haze-free images from Dense-Haze.

For an overall demonstration, we compute the transmission map  $t \in \mathbb{R}^{m \times n \times 3}$  in two different ways (case 1 and case 2 as follows.). For discussion, we first compute the transmission map  $t$  and stack the third-order slice of  $t$  into a matrix  $T$ . Then we verify that the best rank-one approximation  $T_1$  takes the major energy of  $T$ . Note that the energy percentage  $r$  of the obtained rank-one matrix  $T_1$  satisfies  $r = \frac{\|T_1\|_F^2}{\|T\|_F^2} = \frac{\sigma_1^2}{\sum_i \sigma_i^2} \geq 90\%$  with  $\sigma_i, i = 1, 2, 3$ , the singular value of  $T$  [77].

- **Case 1.** Using the physical image formation model (1) to compute  $t$ . Fig. 2 (a) shows the energy percentage of the obtained rank-one approximations from 130 hazy images. In this case, the rank-one transmission energy is higher than 90% of the total energy for over 96% images.
- **Case 2.** Using an existing transmission estimation method [17] to compute  $t$ . Here, we show the energy ratio of the rank-one approximation in Fig. 2 (b). The percentages of all rank-one's approximation energy achieved more than 99.98%.

The results ensure that our proposed rank-one prior is valid for both cases. Then in the following section, we detailedly show how to compute the scattering map  $\tilde{t}$ .

## 4 RECOVERY WITH ROP: IDEAL CASE

For the integrity of this work, we briefly review our preliminary work [14]. Based on the proposed rank-one prior, we seek to compute the scattering map  $\tilde{t}$  by estimating the scattering basis  $b$  and the scattering coefficient  $C$ . Note that our estimation strategy is different from other methods.

### 4.1 Approximation of the basis b

Since the scenes captured using a camera have limited sizes, obtaining the scattering basis  $b$  of the medium from the observed image  $I$  is impossible. Here, we show how to approximate it. Assume that the observed image is uniformly degraded. Eqs. (1) and (2) show that 1) for scenes far from the camera, the obtained image  $I$  is mainly the irradiation of the global ambient light due to the transmission effect; 2) for near scenes, the image contains a relatively small amount of the global ambient light irradiation. The radiation spectrum of imaging contents consists of an environmental scattering spectrum.

For the observed image  $I \in \mathbb{R}^{m \times n \times 3}$ , the unified radiance  $s_u \in \mathbb{R}^3$  is obtained by solving the following minimization problem

$$\min_{s_u} \sum_{x \in \Omega} \|I(x) - s_u^\top\|_2^2, \quad (5)$$

the closed-form solution of (5) can be directly computed as

$$s_u^c = \frac{1}{|\Omega|} \sum_{x \in \Omega} I^c(x), \quad (6)$$

where  $c \in \{R, G, B\}$  is the color channel of  $I$ . The unified radiance reflects the homogeneous ambient light. To describe its essential nature, we normalize the unified radiance as

$$s_{nu} = \frac{s_u}{\|s_u\|_1}. \quad (7)$$

With this normalization, we obtained the unified spectrum  $b \approx s_{nu}$ , which describes the spectral characteristics of the ambient light source. Thus  $s_{nu}$  approximates the common normalized direction for the scattering map. The flowchart in Fig. 3 demonstrates derivations of the approximated unified spectrum using ROP.

### 4.2 Derivation of C

Given the approximation of  $b$ , i.e.,  $b \approx s_{nu}$ , the scattering map  $\tilde{t}$  can be obtained if we have the scattering coefficient  $C$ . Then we have  $\tilde{t}(x) = C(x) \cdot s_{nu}$ . Note that  $\tilde{t}$  should be as close as possible to the observed image  $I$ . Mathematically, we need to minimize the distance between  $I$  and  $\tilde{t}$ . Thus the coefficient vector  $C$  is obtained by solving

$$C(x) = \arg \min_C \sum_{x \in \Omega} \|I(x) - \tilde{t}(x)\|^2 = \langle I(x), s_{nu} \rangle. \quad (8)$$

Then the initial scattering map  $\tilde{t}_0$  satisfies

$$\tilde{t}_0(x) = \langle I(x), s_{nu} \rangle \cdot s_{nu}. \quad (9)$$

This equation implies that  $\tilde{t}_0$  is the projection of  $I$  along the direction  $s_{nu}$ . It holds because the proposed prior depends on the main direction of the observed image intensity, i.e.,

$s_{nu}$ . This novel approach provides a pixel-wise-based estimation strategy and initializes a scattering map involving many details corresponding to imaging contents.

Since the initial scattering map  $\tilde{t}_0$  is obtained by the pixel-to-pixel computation, it presents trivial details of the scenery. If  $\tilde{t}_0$  is used directly for computing the latent scene radiance  $J(x)$ , the contrast of the recovered scene is abnormal. Thus, it is reasonable and necessary to make  $\tilde{t}_0$  in (9) less structured and smoother. Although several methods exist for smoothing  $\tilde{t}_0$ , here, we first downsample and then upsample it, respectively, to obtain a resampled  $\tilde{t}$ , i.e.,

$$\tilde{t} = \text{Resample}(\tilde{t}_0). \quad (10)$$

This direct strategy can get satisfactory results if the degradation is homogeneously distributed. In this work, we use the bilinear interpolation for resampling. The readers are referred to the supplemental materials for the results of different resampling strategies.

The other critical issue is to estimate the ambient light  $A$ . Since the observed pixel correlates with the ambient light, i.e., the pixel with the highest transmission norm is dominated by  $A$ , we first pick the pixels with the top 0.1% norm in  $\tilde{t}$  to avoid outliers and set the mean of these pixels in the observed image  $I$  as the global ambient light  $A$ .

### 4.3 Final recovery formula

From the image formulation model (1) and the estimated scattering map (10), we compute the final latent radiance  $J$  by

$$J(x) = \frac{I(x) - \omega \tilde{t}(x) A}{\max(1 - \omega \tilde{t}(x), \xi)}, \quad (11)$$

where  $\omega \in (0, 1]$  is an introduced constant relaxation parameter and  $\xi$  is the lower bound for a stable computation. Here, we choose  $\xi = 0.001$ . The whole algorithm of the proposed ROP is presented in Algorithm 1.

---

#### Algorithm 1 Rank one prior for the scenery recovery (ROP)

**Input:** Degraded image  $I \in \mathbb{R}^{m \times n \times 3}$ , parameter  $\omega$

**Output:** Recovered image  $J \in \mathbb{R}^{m \times n \times 3}$

- 1: Compute the unified spectrum  $s_{nu}$  using Eq. (7);
  - 2: Compute the scattering map  $\tilde{t}$  using Eq. (10);
  - 3: Downsample  $\tilde{t}$  and then upsample it;
  - 4: Recover the clear image  $J$  using Eq. (11).
- 

### 4.4 Complexity of ROP

The flowchart in Fig. 3 shows that our method is straightforward. There are only several main steps: 1) Use Eq. (6) to compute the mean value of the channel images; 2) Use Eq. (9) to compute the scattering map, and a resampling operation (10) on it; 3) Use Eq. (11) to recover the latent scene  $J$ . All these steps are of complexity  $O(N)$  where  $N$  is the image's size. Hence, the complexity of ROP is  $O(N)$ .

## 5 RECOVERY WITH ROP<sup>+</sup>: GENERAL CASE

In the previous section, we discussed estimating the initial scattering map  $\tilde{t}$  using the whole image pixels. While the reality is that most images have a foreground and background, ROP can not work well in this case. Figs. 5 (b) illustrate these phenomena. Thus, in this section, we propose a new strategy to estimate the scattering map  $\tilde{t}$ .

### 5.1 Improve the unified spectrum $s_{nu}$

In ROP, the unified spectrum  $s_{nu}$  plays a vital role in estimating the scattering map  $\tilde{t}$  of the degraded images captured in various environments. In Fig. 3, we show that ROP uses the whole scene to compute  $s_{nu}$ . The image pixel value for estimating the unified spectrum  $s_{nu}$  should be in roughly the same direction. However, in real scenery, we can not assure that the whole image pixels are similar since the real captured images usually have the depth of field. The effective regions for estimating the unified spectrum  $s_{nu}$  should be in the middle ground and background of the observation.

Here, we discuss how to improve the accuracy of the unified spectrum  $s_{nu}$ . For the observed image  $\mathbf{I} \in \mathbb{R}^{m \times n \times 3}$  and unified radiance  $\mathbf{s}_u \in \mathbb{R}^{1 \times 3}$ , the image pixels for computing the unified radiance  $\mathbf{s}_u$  should not deviate far from the direction of  $\mathbf{s}_u$ , i.e., they should be close enough. We propose to optimize the unified radiance  $\mathbf{s}_u$  by solving the following objective function with a preset constraint,

$$\begin{aligned} \hat{\mathbf{s}}_u = \arg \min_{\mathbf{s}_u} & \sum_{x \in \bar{\Omega}} \|\mathbf{I}(x) - \mathbf{s}_u\|^2, \\ \text{s.t. } & \bar{\Omega} = \{x : \cos \theta_{Is} > \zeta\}, \end{aligned} \quad (12)$$

where  $\theta_{Is}$  is the intersection angle between the vectors  $\mathbf{I}(x)$  and  $\mathbf{s}_u$ . In this paper, we empirically set  $\zeta$  to be 0.99. To solve this problem, we reduced (12) into two subproblems. Thus, for a fixed set  $\bar{\Omega}$  with its initialization  $\Omega$  defined in (5),  $\mathbf{s}_u$  can be computed as follows:

$$\hat{\mathbf{s}}_u^c = \frac{1}{|\bar{\Omega}|} \sum_{x \in \bar{\Omega}} \mathbf{I}^c(x), \quad c \in \{R, G, B\}. \quad (13)$$

Similarly, for a given  $\mathbf{s}_u$  and  $\zeta$ ,  $\bar{\Omega}$  can be obtained accordingly. Both  $\mathbf{s}_u$  and  $\bar{\Omega}$  are updated iteratively. Therefore, we can derive a reasonable corresponding normalized unified spectrum  $s_{nu}$  as

$$\hat{\mathbf{s}}_{nu} = \frac{\hat{\mathbf{s}}_u}{\|\hat{\mathbf{s}}_u\|_1}. \quad (14)$$

In Fig. 3, we show that ROP<sup>+</sup> selects effective regions for estimating the unified spectrum  $s_{nu}$ . In Fig. 4, we show the intermediate results of selected regions in the iterative process. Pixels deviating significantly from the unified radiance  $\mathbf{s}_u$  are excluded (shown in white color).

### 5.2 Improve the scattering coefficient $C$

Physically, the scattering map should preferably be piecewise-smooth in the real scenery. Different from the simple resampling operation in subsection 4.2, we propose

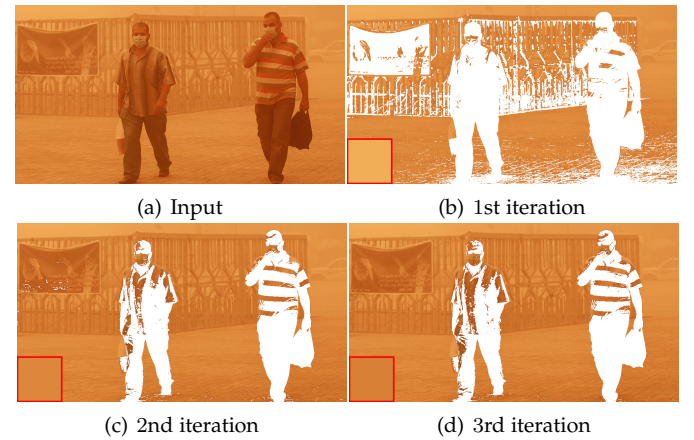


Fig. 4: Selected regions for the unified spectrum computation in the iterative process. The white regions in (b)-(d) are excluded for computing the unified spectrum. The red boxes in the left-bottom corner are the updated unified spectrum.

to optimize the scattering coefficient  $C$  via minimizing the following objective function

$$\begin{aligned} \hat{C} = \arg \min_C & \{\mathcal{E}(C) = \\ & \|C - C_0\|_2^2 + \lambda_1 \|W \circ \nabla(\bar{t} - \mathbf{I})\|_1 + \lambda_2 \|\nabla C\|_1\}, \end{aligned} \quad (15)$$

where  $W(x) = \exp(-\gamma \|\nabla \mathbf{I}(x)\|_1)$  and  $\bar{t}(x) = C(x) \cdot \hat{\mathbf{s}}_{nu}$  for  $x \in \Omega$ ,  $\lambda_1 > 0$  and  $\lambda_2 > 0$  are regularization parameters. The second  $L_1$ -norm regularization controls the mutuality of edges between the image and the scattering map. Since the images reveal many visibly unnecessary details for the scattering map, we introduce a weighting function  $W$  to distinguish the edge and homogeneous regions. A preliminary scattering coefficient  $C_0$  can be estimated pixel-wisely by

$$C_0(x) = \langle \mathbf{I}(x), \hat{\mathbf{s}}_{nu} \rangle, \quad x \in \Omega. \quad (16)$$

Using the unified spectrum  $\hat{\mathbf{s}}_{nu}$ , a preliminary scattering map  $t_0$  is computed by

$$\tilde{t}_0(x) = C_0(x) \cdot \hat{\mathbf{s}}_{nu}, \quad x \in \Omega. \quad (17)$$

The minimization problem (15) can be solved by the alternating direction method of multipliers [78]. A detailed algorithm for solving the minimization problem (15) is provided in the supplemental materials.

As a consequence, the refined scattering map  $\tilde{t}$  is then given by

$$\tilde{t}(x) = \hat{C}(x) \cdot \hat{\mathbf{s}}_{nu}, \quad x \in \Omega. \quad (18)$$

Since we only filter the scattering coefficient  $C$ , the rank one property of the scattering map  $\tilde{t}$  remains valid. To distinguish representations, we use ROP<sup>+</sup> to represent the new method of refining the scattering map  $\tilde{t}$ .

In Fig. 5, the recovered scenes obtained by ROP<sup>+</sup> appear more natural than the ones by ROP. Undoubtedly, this improvement is due to the more accurate scattering map  $\tilde{t}$  obtained using ROP<sup>+</sup>. Compared with ROP, the complexity of ROP<sup>+</sup> is unavoidably higher due to solving the minimization problem (15). At this time, both efficiency and effectiveness may not be attained. The overall procedure is summarized in Algorithm 2.

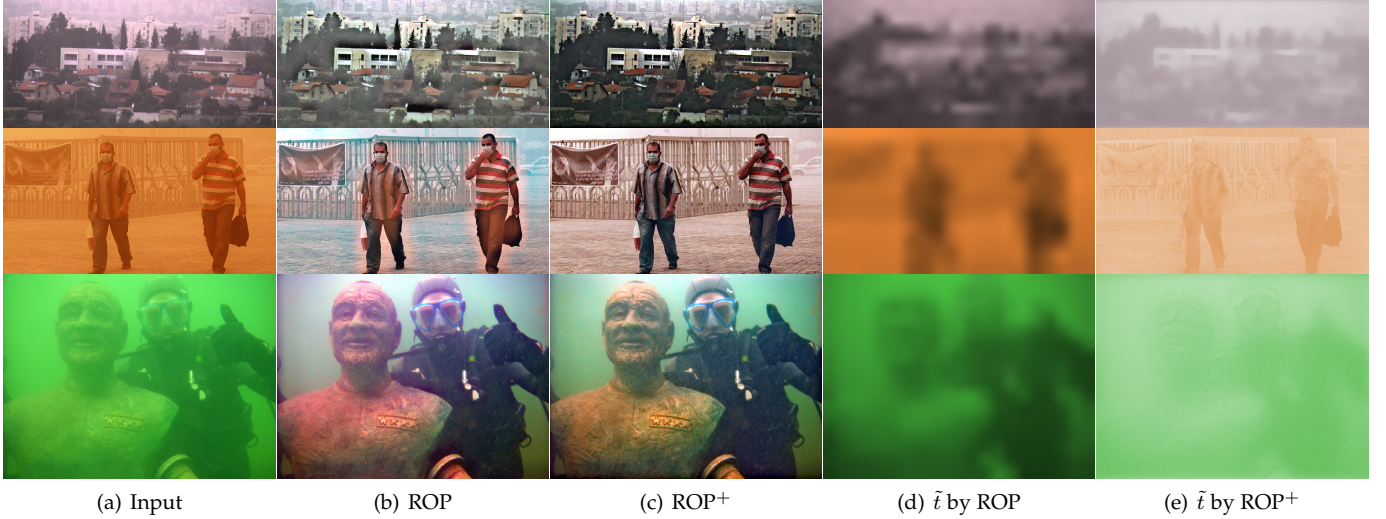


Fig. 5: Comparison between ROP and ROP<sup>+</sup> for the degraded images with parts of scene subjects close to the camera. (The images are best viewed in the full-screen mode.)

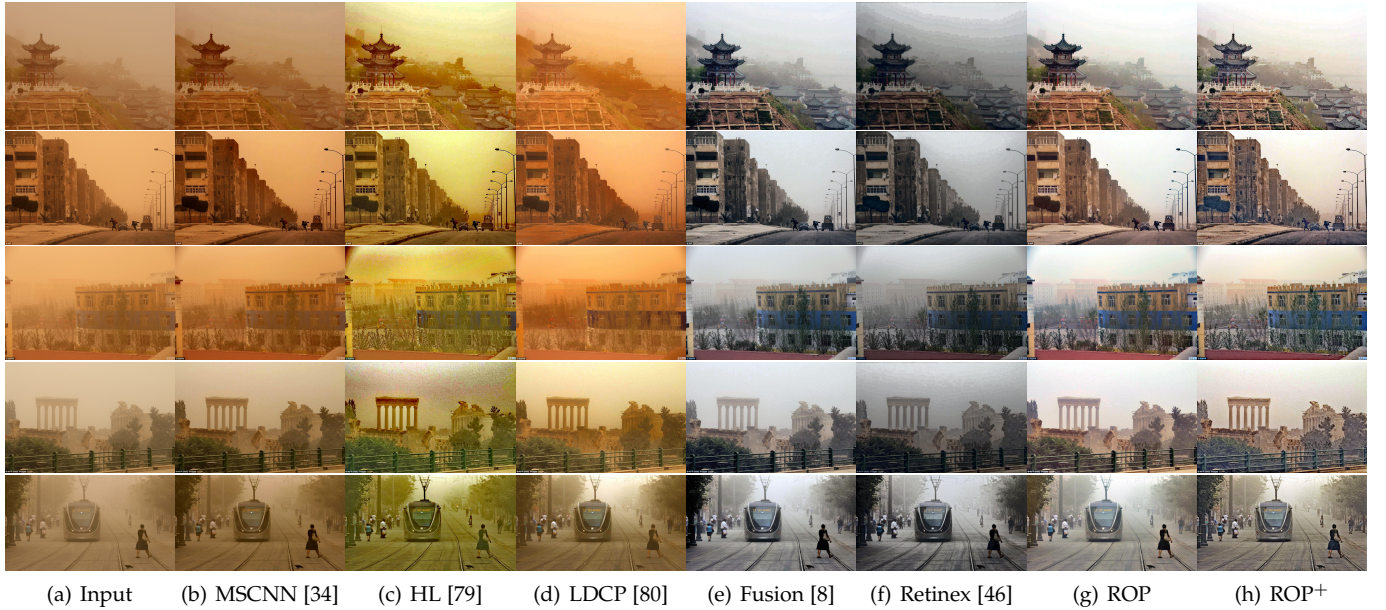


Fig. 6: sand dust image enhancement results obtained using different methods. (The images are best viewed in the full-screen mode.)

#### Algorithm 2 ROP<sup>+</sup> for the scenery recovery

**Input:** Degraded image  $\mathbf{I} \in \mathbb{R}^{m \times n \times 3}$ , parameter  $\omega$

**Output:** Recovered image  $\mathbf{J} \in \mathbb{R}^{m \times n \times 3}$

- 1: Compute the unified spectrum  $\mathbf{s}_{nu}$  using Eq. (14);
- 2: Compute the initial scattering coefficient  $C_0$  by Eq. (16);
- 3: Refine the scattering coefficient  $C$  using Eq. (15);
- 4: Compute the scattering map  $\tilde{t}$  using Eq. (18);
- 5: Recover the clear image  $\mathbf{J}$  using Eq. (11).

## 6 NUMERICAL EXPERIMENTS

This section elaborates on the implementation details and analyzes the imaging results on different exemplary applications of the proposed method, including sand dust image

enhancement, underwater image enhancement, and image dehazing. We show that our unsupervised methods have superiority compared to some supervised deep learning methods.

### 6.1 Implementation

The prominent advantage of our method is that the imaging performance only depends on  $\omega \in (0, 1]$  in Eq. (11). Thus, the estimation of the scattering map  $\tilde{t}$  is parameter-free and robust under different visibility conditions. We conducted numerous experiments to determine the optimal parameter  $\omega$ . This parameter is empirically set as  $\omega = 0.8$ , which guarantees high-quality visual results in most cases. Since  $\omega$  is application-based, readers can try different values for better performance.

All experiments are performed using Matlab R2018a on a machine with an Intel(R) Core (TM) i9-10850K CPU @3.60 GHz. Unless specified, all test images are realistic scenarios collected from the Internet. Our methods are compared with several state-of-the-art methods. For fairness, the competing methods produce the most satisfactory imaging results using the best tuning parameters in this work.

**Run-time performance.** To test the efficiency of different methods on different single image sizes, we showed the run-time of our method on a machine with an NVIDIA GTX 2080Ti GPU (11 GB RAM).

Table 1 shows that our method performs much faster than competitors (even deep learning-based methods). ROP can obtain real-time performance on a moderate-size image with GPU acceleration.

## 6.2 Underwater image enhancement

The realistic underwater images are obtained from a dataset named Underwater Image Enhancement Benchmark (UIEB), and Stereo Quantitative Underwater Image Dataset (SQUID) established by Li et al. [52] and Berman et al. [50], respectively. We compared our method with two-step based method [47], UWCNN [9], and underwater haze line (HL) based method [50]. Fig. 8 (a) is the raw underwater image that seems greenish and blue. Such color deviation affects visual quality. Among these competitors, the two-step method and underwater HL perform better than UWCNN. However, underwater HL performed worse than the two-step method for the last two images. By comparison, our results had better color, sharpness, and contrast. If some portions of the scene object are too close to the camera, ROP<sup>+</sup> outperformed ROP.

Besides the astonishing performance on underwater image enhancement, our method does well in sand dust image enhancement and image dehazing. We present some results in the following subsections.

## 6.3 Visibility restoration in the sand dust weather

First, we validate the effectiveness and robustness of our method for visibility reconstruction in sand dust weather. Sand dust could degrade visibility due to light scattering and absorption by floating sand and dust. It negatively influences practical applications, e.g., video surveillance systems, automatic navigation, remote sensing, etc. The performance of the proposed method is compared with six approaches, namely, DCP [5], MSCNN [34], HL [79], LDCP [80], Fusion [8], and Retinex [46]. Some sand dust images and corresponding restoration results are visually displayed in Fig. 6. Observe that the comparative dehazing methods (i.e., DCP [5], MSCNN [34], HL [13], and LDCP [80]) restore prominent structures but fail to effectively suppress sand dust impacts. Although the Retinex-based method [46] achieves good performance, it has color distortion problems, e.g., inconsistent brightness and loss of textural details, leading to image quality degradation. By comparison, our method produces more natural-looking results with better structures in a more robust manner.

## 6.4 Image and video dehazing

We compare our method with state-of-the-art methods including MSCNN [34], LDCP [80], and AODNet [35]. The test images are obtained from the RESIDE dataset by Li et al. [85]. Fig. 9 shows the comparisons of these different methods. Results obtained by LDCP [80] appear unreal blue. The deep learning-based methods MSCNN [34] and AODNet [35], produce good and stable results. Visually, the dehazed results of our methods are very competitive compared with others. The sky in our results looks more natural and real.

Fig. 10 shows video dehazing results using different methods. We can observe that LDCP is unstable due to the saturation changes in different frames. DCP, MSCNN, and AODNet also can not work well. Compared with other methods, both ROP and ROP<sup>+</sup> are more stable and produce better results. If the readers want to know in-depth about video dehazing, please refer to [86].

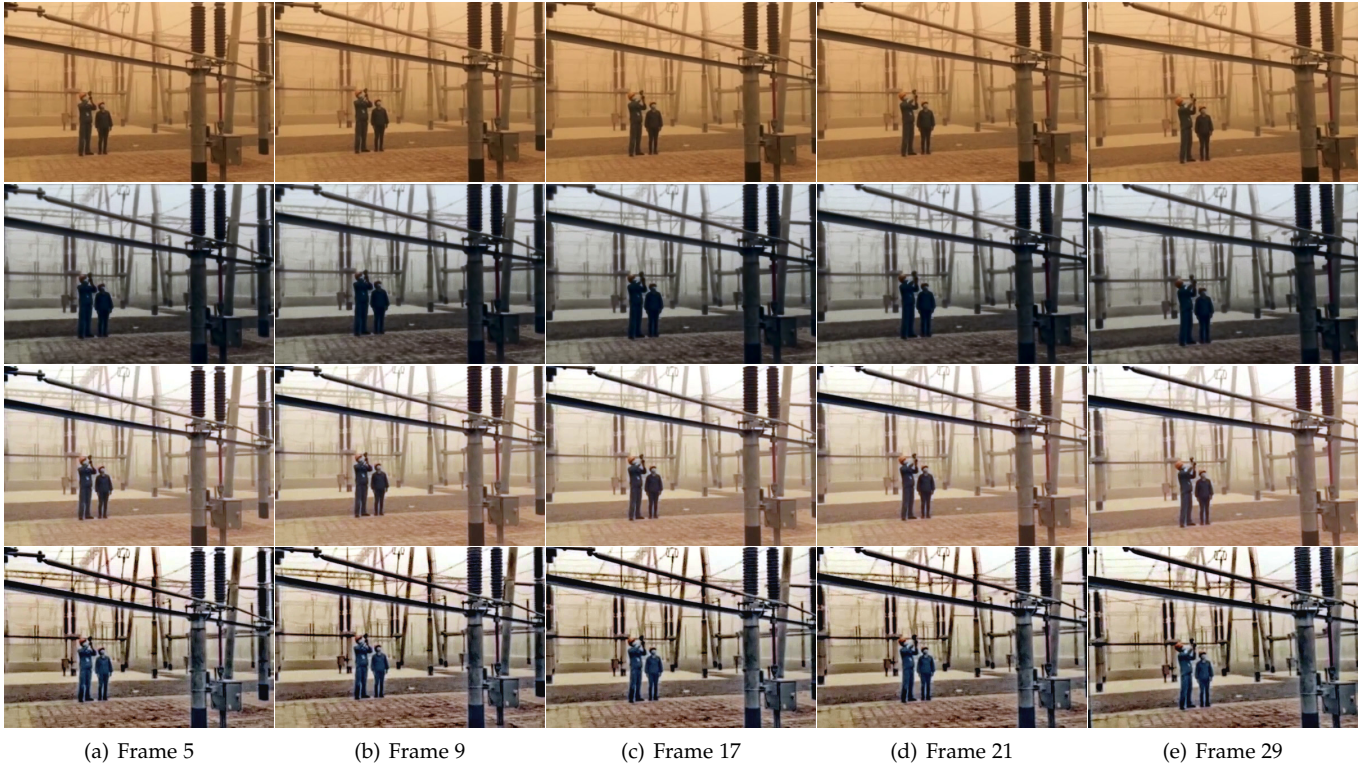
To objectively evaluate the performance of the proposed method, we compared our method with several deep-learning-based methods and model-based methods with a hazy synthetic dataset OTS [85]. The PSNR results are shown in Table 2. Indeed, some state-of-the-art deep learning-based methods, such as GridDehazeNet [84], and FFANet [82], do have their superiority over our proposed methods. To the best of our knowledge, deep learning-based methods sometimes suffer from robustness and generalization. While our methods are robust in real image dehazing. For real hazy images, In Fig. 11, we compare ROP and ROP<sup>+</sup> with several deep learning-based methods such as AODNet [35], CAP [81], MSCNN [34], DehazeNet [33], FFANet [82], GCANet [83], GridDehazeNet [84] and the model-based methods such as HL [13] and LDCP [80]. We can observe that the proposed ROP<sup>+</sup> can provide much better results than others.

We further present a classic example in Fig. 12 which was compared with MSCNN [34] and HL [13]. It is easy to check that ROP<sup>+</sup> provides a competitive comparison result. We also compare our methods with a DCP-based optimization method [87] and a robust dehazing method proposed by Chen et al. [88]. Instead of directly reconstructing clear images using the hazy model (1), the authors proposed to recover the clear image by solving a minimization problem. Their model measures the dark channel using  $L_0$  sparsity. The results shown in Fig. 13 show that our methods restore much clearer and more detailed results. Overall, our approaches outperform their methods by producing much more accurate scene recovery. Furthermore, our methods can also work well for purple hazy image recovery. From Fig. 14, the examples of purple haze removal effectively verified the capability of our methods.

## 7 NON-REFERENCE QUALITY ASSESSMENT

To benefit the academic and industrial research, we collect a dataset with Real Underwater, Sand dust, and Hazy images (RUSH)<sup>b</sup> from the internet. This RUSH set has 250 images, including 50 underwater images, 100 hazy images, and 100 sand dust images. Samples of RUSH are shown in Fig. 15.

b. It is available in <https://www.dropbox.com/sh/vsexfpemi36fv7d/AAC3FCIZaulZPoWxZtTcLFAAa?dl=0>



(a) Frame 5

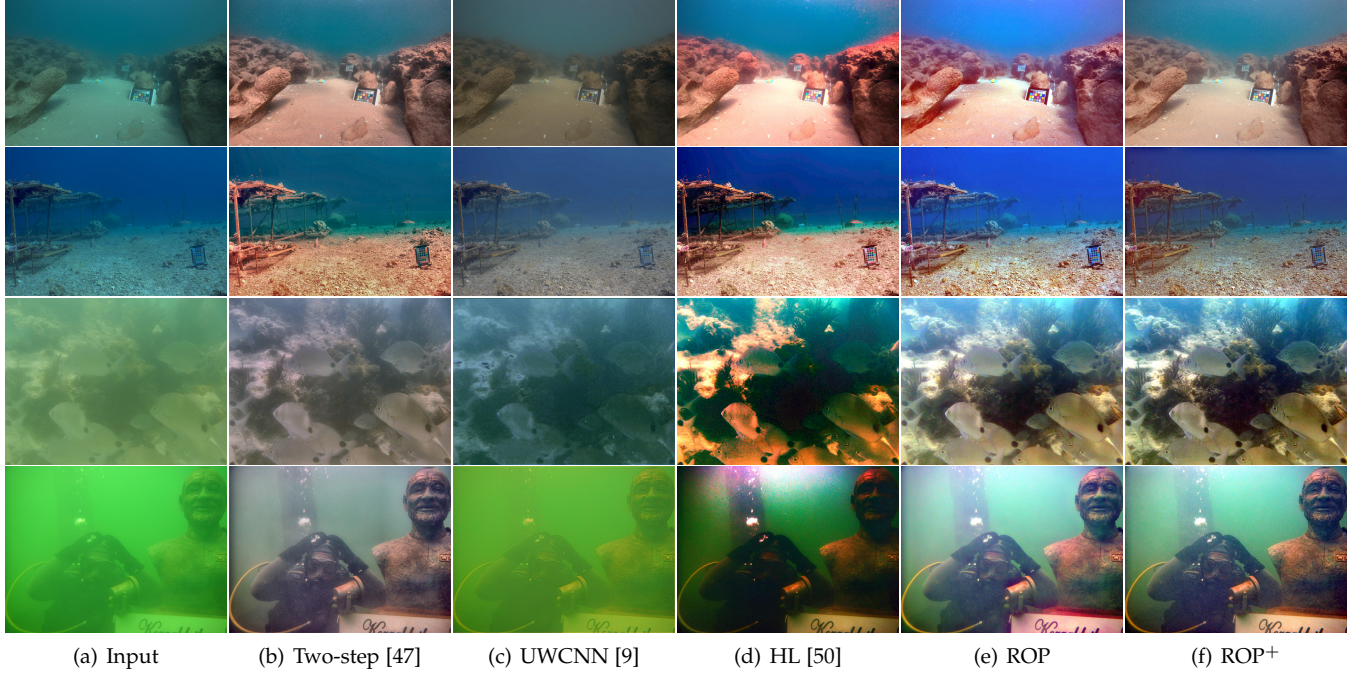
(b) Frame 9

(c) Frame 17

(d) Frame 21

(e) Frame 29

Fig. 7: Sand dust video enhancement results obtained using different methods. The first row presents the input frames; The second row is the corresponding enhanced results using Fu et al. [46]'s method; The third row is the results using ROP. The last row is the results using ROP<sup>+</sup>. (The images are best viewed in the full-screen mode.)



(a) Input

(b) Two-step [47]

(c) UWCNN [9]

(d) HL [50]

(e) ROP

(f) ROP<sup>+</sup>

Fig. 8: Enhanced results of underwater images obtained using different methods. (The images are best viewed in the full-screen mode.)

Note that there are some related datasets, such as RTTS (Real-world Task-driven Testing Set) released by Li et al. [85] and SQUID (Stereo Quantitative Underwater Image Dataset) released by Berman et al. [50]. More recently, Si

et al. [62] introduced a synthetic SIRB (Sand-dust Image Reconstruction Benchmark) and a collected RSTS (Real-world Sandstorm Testing Set). Since our methods are essentially multi-purpose methods for real degraded image enhance-

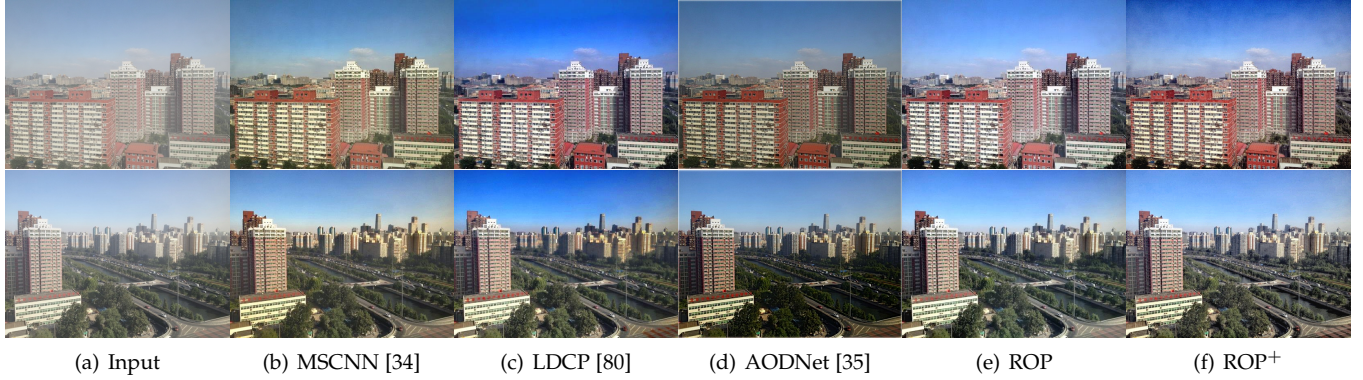


Fig. 9: Dehazing results obtained using different methods. (The images are best viewed in the full-screen mode.)

TABLE 1: Run-time (seconds) performance. All methods were tested on the same machine using the same test images. ROP can reach real-time performance for the moderate image size using GPU (Nvidia 2080Ti). Without specification, all methods were performed using CPU (Intel(R) Core(TM) i9-10850K CPU @3.60 GHz).

Size	DCP [5]	LDCP [80]	Fusion [8]	MSCNN [34]	HL [79]	DehazeNet [33]	AODNet [35]	CAP [81]	ROP	ROP (GPU)	ROP <sup>+</sup>
360p	0.47	0.44	0.28	0.55	0.39	0.85	0.36	0.54	0.05	0.04	0.18
480p	0.95	0.86	0.54	0.98	0.83	1.88	0.70	0.78	0.12	0.04	0.29
720p	2.51	2.29	1.57	2.48	2.47	6.01	1.84	1.56	0.33	0.07	0.69
1080p	5.71	5.11	3.70	5.62	5.98	14.89	4.34	3.11	0.80	0.12	1.50
2k	10.15	9.34	6.75	11.22	11.20	27.33	8.07	6.80	1.47	0.18	2.68
4k	27.75	25.42	18.60	30.90	35.54	76.22	21.72	13.55	4.05	0.46	6.57

TABLE 2: Objective evaluation on OTS [85].

Method	PSNR	Method	PSNR
Hazy	13.27	GCANet [83]	21.83
DCP [5]	16.91	GridDehazeNet [84]	24.10
CAP [81]	19.54	FFANet [82]	19.60
HL [13]	17.94	DehazeNet [33]	23.09
MSCNN [34]	18.26	ROP	18.10
AODNet [35]	18.61	ROP <sup>+</sup>	19.35

ment, we wish to collect the corresponding different types of degraded images in one dataset. As several test images commonly appeared in many related published papers, our dataset also includes them. Our dataset mainly contains three types of degraded images, i.e., underwater images, sand dust images, and hazy images. It differs significantly from previous datasets containing one specific type of degraded images.

Since there are no ground-truth images corresponding to the dataset RUSH, we can not compute the PSNR or SSIM of the recovered images. Thus, two well-known non-reference indexes NIQE (Natural Image Quality Evaluator [15]) and PIQE (Perception-based Image Quality Evaluator [16]) are utilized for quality assessment. Generally, lower NIQE and PIQE scores represent better recovery evaluation.

We compare ROP<sup>+</sup> with different methods for different types of degradation. For underwater images, the algorithms for comparison are MILHD (Minimum Information Loss and Histogram Distribution Prior) [89], Retinex [46], Two-Step [47], UBLA (Underwater image recovery using image Blurriness and Light Absorption) [90] and ROP [14].

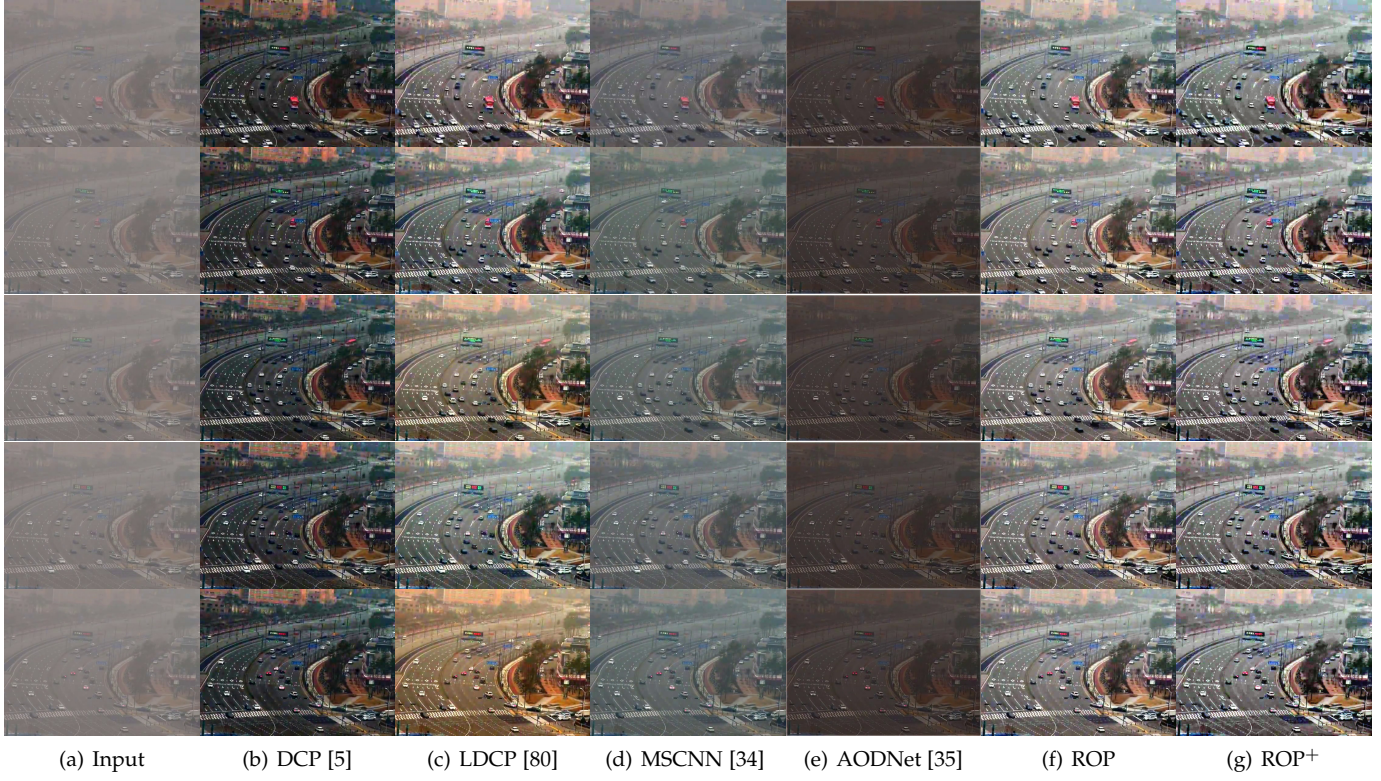
For sand dust images, the algorithms for comparison are HL method [13], DCP [5], LDCP [80], Retinex [46], Fusion [8] and ROP [14]. For hazy images, the algorithms for comparison are DCP [5], HL [13], LDCP [80], MSCNN [34], AODNet [35] and ROP [14]. The objective image quality assessments are shown in Table 3-5. Since NIQE and PIQE are not in the same order of magnitude, it may be unfair to compare their averages for different methods. To this end, we scale these values to [0, 1], where 0 represents the best performance, and 1 means the worst performance. We can check that ROP<sup>+</sup> has superior performance. These objective assessments verify the robustness and effectiveness of our method.

## 8 EXTENSION

In this section, we extend our methods for image low-light enhancement. Low-light images often suffer from low contrast and poor visibility, etc. Many image enhancement algorithms, such as [91], [92], [93], [94], [95], were proposed using Retinex model. Interestingly, the connection between image dehazing and Retinex was established by Galdran et al. [96] in 2018. Suppose that  $\mathcal{T}_d$  and  $\mathcal{T}_r$  are the dehazing and Retinex operators. For pixel values of the input degraded image  $I$  scaled within the range [0, 1], Galdran et al. [96] derived that

$$\mathcal{T}_r(\mathbf{I}) = 1 - \mathcal{T}_d(1 - \mathbf{I}). \quad (19)$$

From this linear relationship between dehazing and Retinex, we can directly apply our methods for low-light image enhancement. In Fig. 16(a), we presented an example using real low-light image captured by a mobile phone. The enhanced results in Fig. 16(b), (c) and (d) show that the proposed methods are attractively suitable for Retinex. We



(a) Input      (b) DCP [5]      (c) LDCCP [80]      (d) MSCNN [34]      (e) AODNet [35]      (f) ROP      (g) ROP<sup>+</sup>

Fig. 10: (a) Different frames from a hazy video; (b)-(f) Dehazed results corresponding to (a) obtained by different methods. (The images are best viewed in the full-screen mode.)



Fig. 11: Real hazy images recovery: Comparisons of our methods ROP and ROP<sup>+</sup> with the deep learning-based methods AODNet [35], CAP [81], MSCNN [34], DehazeNet [33], FFANet [82], GCANet [83], GridDehazeNet [84] and the model-based methods HL [13] and DCP [5].



Fig. 12: Natural hazy image: Dehazed results obtained using different methods. (The images are best viewed in the full-screen mode.)

TABLE 3: The image enhancement quality assessment of 50 real **underwater** images in RUSH by different methods. The NIQE and PIQE scores are the average scores of all enhanced images. The AVERAGE score is the mean of NIQE and PIQE scores. The numbers in parentheses are scaled scores. (Bold values indicate the best methods. )

Method \ Metric	Retinex [46]	MILHD [89]	Two-step [47]	UBLA [90]	ROP	ROP <sup>+</sup>
PIQE ↓	29.61(1.00)	13.48 (0.04)	12.82 (0.01)	17.18 (0.26)	18.10 (0.32)	<b>12.74 (0.00)</b>
NIQE ↓	3.80 (1.00)	3.61 (0.65)	3.30 (0.07)	3.70 (0.82)	3.40 (0.26)	<b>3.26 (0.00)</b>
Average	1	0.35	0.04	0.54	0.29	<b>0.00</b>

TABLE 4: The image enhancement quality assessment of 100 real **sand dust** images in RUSH by different methods. The NIQE and PIQE scores are the average scores of all enhanced images. The AVERAGE score is the mean of NIQE and PIQE scores. The numbers in parentheses are scaled scores. (Bold values indicate the best methods.)

Method \ Metric	DCP [5]	LDCP [80]	Fusion [8]	HL [13]	Retinex [46]	ROP	ROP <sup>+</sup>
PIQE ↓	22.16 (0.38)	24.88 (0.52)	19.25 (0.22)	18.61 (0.18)	33.81 (1.00)	19.31 (0.22)	<b>15.31 (0.00)</b>
NIQE ↓	3.98 (0.77)	4.15 (1.00)	3.71 (0.40)	3.62 (0.28)	4.10 (0.94)	3.66 (0.33)	<b>3.42 (0.00)</b>
Average	0.57	0.76	0.31	0.23	0.97	0.28	<b>0.00</b>

TABLE 5: The image enhancement quality assessment of 100 real **hazy** image in RUSH by different methods. The NIQE and PIQE scores are the average scores of all enhanced images. The AVERAGE score is the mean of NIQE and PIQE scores. The numbers in parentheses are scaled scores. (Bold values indicate the best methods. )

Method \ Metric	AODNet [35]	DCP [5]	LDCP [80]	MSCNN [34]	HL [13]	ROP	ROP <sup>+</sup>
PIQE ↓	23.21 (0.92)	17.92 (0.49)	20.95 (0.74)	24.21 (1.00)	15.81 (0.32)	17.41 (0.45)	<b>11.92 (0.00)</b>
NIQE ↓	4.29 (1.00)	3.70 (0.44)	3.91 (0.65)	4.13 (0.85)	3.47 (0.23)	3.60 (0.36)	<b>3.42 (0.00)</b>
Average	0.96	0.47	0.70	0.93	0.28	0.41	<b>0.00</b>

claim that this example is to demonstrate our method can be used for low-light image enhancement only.

## 9 ANALYSIS AND DISCUSSION

Both ROP and ROP<sup>+</sup> provide a good guidance for computing the scattering map by projecting the observed spectrum onto the unified spectrum. We derive the scattering map  $\tilde{t}$  from the ambient light instead of computing the transmission  $t$  from the scene radiance. Using statistical validation on real haze datasets, we introduce rank-one prior and unified spectrum to de- scribe and measure the ambient-light-based transmission. Hence, we approximate the transmission linearly by the unified spectrum for each pixel. Our approaches have some relations with other methods.

### 9.1 Relation with other methods

#### 9.1.1 Relation with DCP [97]

Both DCP and our method use physical assumptions, i.e., both priors can be supported by statistical verification. However, DCP is prior for the natural image, whereas ours is for the ambient light. Since the transmission computed by DCP is only one single channel, DCP prior satisfies our ROP by setting the three channels equal.

#### 9.1.2 Relation with AWB

Additionaly, our method is related to some automatic white balancing (AWB) algorithms. Estimating  $s_u$  is similar to the gray world (GW) [98], which requires illumination estimation. In GW, the mean of the r, g, b channels in a given scene should be roughly equal. It computes the average of the red, green, and blue color components, respectively.

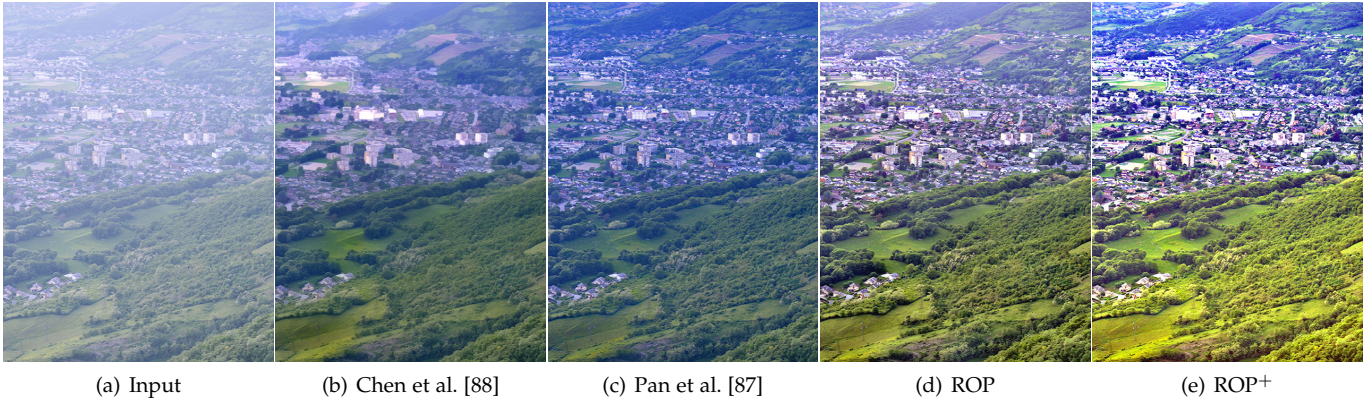


Fig. 13: ROP and ROP<sup>+</sup> for natural image dehazing. The dehazed image (d) and (e) obtained using our methods are clearer and contain more details compared to the results in (b) and (c). ROP<sup>+</sup> has better performance than ROP. Note that (a)-(c) are obtained directly from Pan et al.'s publication [87].

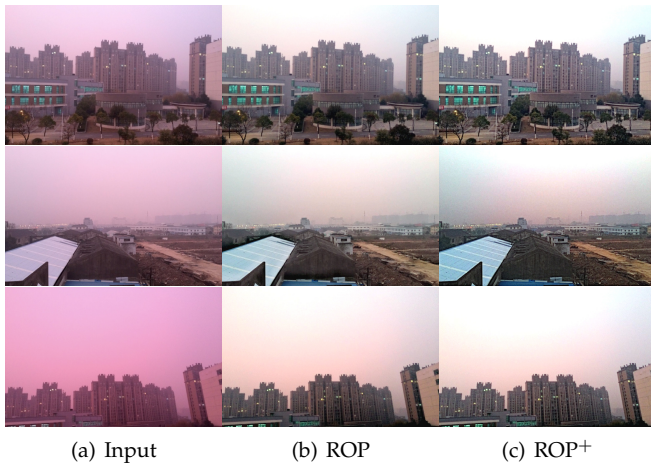


Fig. 14: (a) Purple hazy images captured in the winter of Nanjing, China, 22 December 2015. (b) Dehazed images obtained using ROP and ROP<sup>+</sup>.



Fig. 15: Samples from the RUSH dataset.

#### 9.1.3 Relation with Color-line [27]

Fattal [27] assumed that many small image patches corresponded to mono-chromatic surfaces and admitted

$$\mathbf{J}(x) = \ell(x)\bar{\mathbf{R}}, x \in \Omega(y), \quad (20)$$

where  $\Omega(y)$  is a local patch corresponding to the pixel  $y$ ,  $\bar{\mathbf{R}}$  is the relative intensity of each color channel of the reflected light, i.e.,  $\|\bar{\mathbf{R}}\| = 1$ . The scalar  $\ell(x)$  describes the magnitude of the radiance at each pixel  $x$  in the patch  $\Omega(y)$ . In this respect,  $\mathbf{J}$  is a rank one matrix (with unfolding) in a patch and similar to the proposed scattering map estimation.

## 9.2 Limitations

Since the whole degraded image was used to obtain the unified spectrum, the result may not be good enough if the distance between nearby and distant objects is too large. A possible solution is to use a supervised strategy, i.e., selecting a good region to obtain the unified spectrum. Another potential problem is that originally unnoticeable impurities, such as noise and blocking artifacts, will be amplified [88], [99]. These artifacts can be observed in Fig. 17. For denoising problems, we could resort to using some successful denoising methods in the past two years for post-processing, such as a variational denoising network [100]. Furthermore, we can use multispectral joint image restoration, such as using the color and near-infrared images captured in the haze [101]. Interestingly, our method can be applied to foreground and background separation in bad weather [102]. Several demonstrations are presented in the supplemental materials.

## 10 CONCLUSION

The main idea of the proposed ROP considers an intensity projection strategy for estimating the scattering map. The complexity of the scattering map estimation is  $O(N)$ , where  $N$  is a single image's size. We also introduce some limitations of ROP and proposed a new method called ROP<sup>+</sup> which can improving upon performance of ROP. The scene recovery results obtained by the proposed approach are very competitive with the state-of-the-art methods. The advantages of our method are reflected in its strong universality, and adaptability to deal with different scene restoration problems. Most recent deep learning methods can only solve a specific task. Our methods may provide a direction for the portability of these deep learning methods. Notably, since sand dust image enhancement research remains less than other topics discussed in this paper, our work would be a good starting point. More results can be found in the supplemental materials.

## REFERENCES

- [1] Y. Pei, Y. Huang, Q. Zou, X. Zhang, and S. Wang, "Effects of image degradation and degradation removal to CNN-based



Fig. 16: ROP and ROP<sup>+</sup> for the real captured image Retinex. (b) is obtained by adjusting the input levels using Photoshop.



Fig. 17: Limitations. The unnoticeable artifacts such as jpeg-blocks and noise in the degraded images are greatly magnified after image enhancing using ROP and ROP<sup>+</sup>. The second and third rows are the results using ROP and ROP<sup>+</sup>, respectively. (The images are best viewed in the full-screen mode.)

- [2] R. W. Liu, W. Yuan, X. Chen, and Y. Lu, "An enhanced CNN-enabled learning method for promoting ship detection in maritime surveillance system," *Ocean Engineering*, vol. 235, p. 109435, 2021.
- image classification," *IEEE Transactions on Pattern Analysis and Machine Intelligence*, vol. 43, no. 4, pp. 1239–1253, 2021.

- [3] K. B. Gibson, D. T. Vo, and T. Q. Nguyen, "An investigation of dehazing effects on image and video coding," *IEEE Transactions on Image Processing*, vol. 21, no. 2, pp. 662–673, 2012.
- [4] W. Ren, J. Zhang, X. Xu, L. Ma, X. Cao, G. Meng, and W. Liu, "Deep video dehazing with semantic segmentation," *IEEE Transactions on Image Processing*, vol. 28, no. 4, pp. 1895–1908, 2019.
- [5] K. He, J. Sun, and X. Tang, "Single image haze removal using dark channel prior," *IEEE Transactions on Pattern Analysis and Machine Intelligence*, vol. 33, no. 12, pp. 2341–2353, 2011.
- [6] M. Sulami, I. Glatzer, R. Fattal, and M. Werman, "Automatic recovery of the atmospheric light in hazy images," in *IEEE International Conference on Computational Photography (ICCP)*, 2014, pp. 1–11.
- [7] F. Fang, F. Li, and T. Zeng, "Single image dehazing and denoising: a fast variational approach," *SIAM Journal on Imaging Sciences*, vol. 7, no. 2, pp. 969–996, 2014.
- [8] X. Fu, Y. Huang, D. Zeng, X.-P. Zhang, and X. Ding, "A fusion-based enhancing approach for single sandstorm image," in *IEEE 16th International Workshop on Multimedia Signal Processing (MMSP)*, 2014, pp. 1–5.
- [9] C. Li, S. Anwar, and F. Porikli, "Underwater scene prior inspired deep underwater image and video enhancement," *Pattern Recognition*, vol. 98, p. 107038, 2020.
- [10] Y. Y. Schechner and Y. Averbuch, "Regularized image recovery in scattering media," *IEEE Transactions on Pattern Analysis and Machine Intelligence*, vol. 29, no. 9, pp. 1655–1660, 2007.
- [11] Y.-T. Peng, K. Cao, and P. C. Cosman, "Generalization of the dark channel prior for single image restoration," *IEEE Transactions on Image Processing*, vol. 27, no. 6, pp. 2856–2868, 2018.
- [12] Y. Y. Schechner, S. G. Narasimhan, and S. K. Nayar, "Instant dehazing of images using polarization," in *Proceedings of the IEEE Conference on Computer Vision and Pattern Recognition (CVPR)*. IEEE, 2001, pp. I-325–I-332.
- [13] D. Berman, T. Treibitz, and S. Avidan, "Single image dehazing using haze-lines," *IEEE Transactions on Pattern Analysis and Machine Intelligence*, vol. 42, no. 3, pp. 720–734, 2018.
- [14] J. Liu, W. Liu, J. Sun, and T. Zeng, "Rank-one prior: Toward real-time scene recovery," in *Proceedings of the IEEE Conference on Computer Vision and Pattern Recognition (CVPR)*, 2021, pp. 14 802–14 810.
- [15] A. Mittal, R. Soundararajan, and A. C. Bovik, "Making a "completely blind" image quality analyzer," *IEEE Signal Processing Letters*, vol. 20, no. 3, pp. 209–212, 2013.
- [16] N. Venkatanath, D. Praneeth, M. C. Bh, S. S. Channappayya, and S. S. Medasani, "Blind image quality evaluation using percep-

- tion based features," in *2015 Twenty First National Conference on Communications (NCC)*. IEEE, 2015, pp. 1–6.
- [17] Q. Shu, C. Wu, Z. Xiao, and R. W. Liu, "Variational regularized transmission refinement for image dehazing," in *IEEE International Conference on Image Processing (ICIP)*, 2019, pp. 2781–2785.
- [18] S. G. Narasimhan and S. K. Nayar, "Vision and the atmosphere," *International Journal of Computer Vision*, vol. 48, no. 3, pp. 233–254, 2002.
- [19] ——, "Contrast restoration of weather degraded images," *IEEE Transactions on Pattern Analysis and Machine Intelligence*, vol. 25, no. 6, pp. 713–724, 2003.
- [20] R. Fattal, "Single image dehazing," *ACM Transactions on Graphics (TOG)*, vol. 27, no. 3, pp. 1–9, 2008.
- [21] R. T. Tan, "Visibility in bad weather from a single image," in *Proceedings of the IEEE Conference on Computer Vision and Pattern Recognition (CVPR)*, 2008, pp. 1–8.
- [22] F. Fang, T. Wang, Y. Wang, T. Zeng, and G. Zhang, "Variational single image dehazing for enhanced visualization," *IEEE Transactions on Multimedia*, vol. 22, no. 10, pp. 2537–2550, 2020.
- [23] G. Meng, Y. Wang, J. Duan, S. Xiang, and C. Pan, "Efficient image dehazing with boundary constraint and contextual regularization," in *Proceedings of the IEEE International Conference on Computer Vision (ICCV)*, 2013, pp. 617–624.
- [24] S.-C. Huang, B.-H. Chen, and W.-J. Wang, "Visibility restoration of single hazy images captured in real-world weather conditions," *IEEE Transactions on Circuits and Systems for Video Technology*, vol. 24, no. 10, pp. 1814–1824, 2014.
- [25] K. Tang, J. Yang, and J. Wang, "Investigating haze-relevant features in a learning framework for image dehazing," in *Proceedings of the IEEE Conference on Computer Vision and Pattern Recognition (CVPR)*, 2014, pp. 2995–3000.
- [26] A. Golts, D. Freedman, and M. Elad, "Unsupervised single image dehazing using dark channel prior loss," *IEEE Transactions on Image Processing*, vol. 29, pp. 2692–2701, 2019.
- [27] R. Fattal, "Dehazing using color-lines," *ACM Transactions on Graphics (TOG)*, vol. 34, no. 1, pp. 1–14, 2014.
- [28] Q. Zhu, J. Mai, and L. Shao, "A fast single image haze removal algorithm using color attenuation prior," *IEEE Transactions on Image Processing*, vol. 24, no. 11, pp. 3522–3533, 2015.
- [29] D. Berman, S. Avidan *et al.*, "Non-local image dehazing," in *Proceedings of the IEEE Conference on Computer Vision and Pattern Recognition (CVPR)*, 2016, pp. 1674–1682.
- [30] T. M. Bui and W. Kim, "Single image dehazing using color ellipsoid prior," *IEEE Transactions on Image Processing*, vol. 27, no. 2, pp. 999–1009, 2018.
- [31] M. Kaur, D. Singh, V. Kumar, and K. Sun, "Color image dehazing using gradient channel prior and guided  $l_0$  filter," *Information Sciences*, vol. 521, pp. 326–342, 2020.
- [32] M. Ju, C. Ding, Y. J. Guo, and D. Zhang, "IDGCP: Image dehazing based on gamma correction prior," *IEEE Transactions on Image Processing*, vol. 29, pp. 3104–3118, 2019.
- [33] B. Cai, X. Xu, K. Jia, C. Qing, and D. Tao, "DehazeNet: An end-to-end system for single image haze removal," *IEEE Transactions on Image Processing*, vol. 25, no. 11, pp. 5187–5198, 2016.
- [34] W. Ren, S. Liu, H. Zhang, J. Pan, X. Cao, and M.-H. Yang, "Single image dehazing via multi-scale convolutional neural networks," in *Proceedings of the European Conference on Computer Vision (ECCV)*. Springer, 2016, pp. 154–169.
- [35] B. Li, X. Peng, Z. Wang, J. Xu, and D. Feng, "AOD-Net: All-in-one dehazing network," in *Proceedings of the IEEE International Conference on Computer Vision (ICCV)*, 2017, pp. 4770–4778.
- [36] D. Yang and J. Sun, "Proximal Dehaze-Net: A prior learning-based deep network for single image dehazing," in *Proceedings of the European Conference on Computer Vision (ECCV)*, 2018, pp. 702–717.
- [37] H. Wu, Y. Qu, S. Lin, J. Zhou, R. Qiao, Z. Zhang, Y. Xie, and L. Ma, "Contrastive learning for compact single image dehazing," in *Proceedings of the IEEE Conference on Computer Vision and Pattern Recognition (CVPR)*, 2021, pp. 10551–10560.
- [38] Q. Deng, Z. Huang, C.-C. Tsai, and C.-W. Lin, "HardGAN: A haze-aware representation distillation gan for single image dehazing," in *Proceedings of the European Conference on Computer Vision (ECCV)*. Springer, 2020, pp. 722–738.
- [39] Y. Qu, Y. Chen, J. Huang, and Y. Xie, "Enhanced pix2pix dehazing network," in *Proceedings of the IEEE Conference on Computer Vision and Pattern Recognition (CVPR)*, 2019, pp. 8160–8168.
- [40] X. Liu, Z. Gao, and B. M. Chen, "MLFcGAN: Multilevel feature fusion-based conditional gan for underwater image color correction," *IEEE Geoscience and Remote Sensing Letters*, vol. 17, no. 9, pp. 1488–1492, 2019.
- [41] C. Ancuti, C. O. Ancuti, T. Haber, and P. Bekaert, "Enhancing underwater images and videos by fusion," in *Proceedings of the IEEE International Conference on Computer Vision (ICCV)*, 2012, pp. 81–88.
- [42] C. O. Ancuti, C. Ancuti, C. De Vleeschouwer, and P. Bekaert, "Color balance and fusion for underwater image enhancement," *IEEE Transactions on Image Processing*, vol. 27, no. 1, pp. 379–393, 2017.
- [43] L. Chao and W. Meng, "Removal of water scattering," in *International Conference on Computer Engineering and Technology*, vol. V2, 2010, pp. 35–39.
- [44] J. P. Drews, E. Nascimento, F. Moraes, S. Botelho, and M. Campos, "Transmission estimation in underwater single images," in *IEEE International Conference on Computer Vision Workshops*, 2013, pp. 825–830.
- [45] P. J. Drews, E. R. Nascimento, S. S. Botelho, and M. F. M. Campos, "Underwater depth estimation and image restoration based on single images," *IEEE Computer Graphics and Applications*, vol. 36, no. 2, pp. 24–35, 2016.
- [46] X. Fu, P. Zhuang, Y. Huang, Y. Liao, X.-P. Zhang, and X. Ding, "A retinex-based enhancing approach for single underwater image," in *2014 IEEE International Conference on Image Processing (ICIP)*, 2014, pp. 4572–4576.
- [47] X. Fu, Z. Fan, M. Ling, Y. Huang, and X. Ding, "Two-step approach for single underwater image enhancement," in *2017 International Symposium on Intelligent Signal Processing and Communication Systems (ISPACS)*, 2017, pp. 789–794.
- [48] J. Y. Chiang and Y.-C. Chen, "Underwater image enhancement by wavelength compensation and dehazing," *IEEE Transactions on Image Processing*, vol. 21, no. 4, pp. 1756–1769, 2012.
- [49] S.-B. Gao, M. Zhang, Q. Zhao, X.-S. Zhang, and Y.-J. Li, "Underwater image enhancement using adaptive retinal mechanisms," *IEEE Transactions on Image Processing*, vol. 28, no. 11, pp. 5580–5595, 2019.
- [50] D. Berman, D. Levy, S. Avidan, and T. Treibitz, "Underwater single image color restoration using haze-lines and a new quantitative dataset," *IEEE Transactions on Pattern Analysis and Machine Intelligence*, vol. 43, no. 08, pp. 2822–2837, 2021.
- [51] A. Jamadandi and U. Mudenagudi, "Exemplar-based underwater image enhancement augmented by wavelet corrected transforms," in *Proceedings of the IEEE Conference on Computer Vision and Pattern Recognition Workshops (CVPRW)*, 2019, pp. 11–17.
- [52] C. Li, C. Guo, W. Ren, R. Cong, J. Hou, S. Kwong, and D. Tao, "An underwater image enhancement benchmark dataset and beyond," *IEEE Transactions on Image Processing*, vol. 29, pp. 4376–4389, 2019.
- [53] Y. Guo, H. Li, and P. Zhuang, "Underwater image enhancement using a multiscale dense generative adversarial network," *IEEE Journal of Oceanic Engineering*, vol. 45, no. 3, pp. 862–870, 2020.
- [54] H. Li and P. Zhuang, "DewaterNet: A fusion adversarial real underwater image enhancement network," *Signal Processing: Image Communication*, vol. 95, p. 116248, 2021.
- [55] S. Anwar and C. Li, "Diving deeper into underwater image enhancement: A survey," *Signal Processing: Image Communication*, vol. 89, p. 115978, 2020.
- [56] R. Liu, X. Fan, M. Zhu, M. Hou, and Z. Luo, "Real-world underwater enhancement: Challenges, benchmarks, and solutions under natural light," *IEEE Transactions on Circuits and Systems for Video Technology*, vol. 30, no. 12, pp. 4861–4875, 2020.
- [57] J. Wang, Y. Pang, Y. He, and C. Liu, "Enhancement for dust-sand storm images," in *International Conference on Multimedia Modeling*. Springer, 2016, pp. 842–849.
- [58] Y. Yang, C. Zhang, L. Liu, G. Chen, and H. Yue, "Visibility restoration of single image captured in dust and haze weather conditions," *Multidimensional Systems and Signal Processing*, vol. 31, no. 2, pp. 619–633, 2020.
- [59] Y. Cheng, Z. Jia, H. Lai, J. Yang, and N. K. Kasabov, "A fast sand-dust image enhancement algorithm by blue channel compensation and guided image filtering," *IEEE Access*, vol. 8, pp. 196690–196699, 2020.
- [60] B. Wang, B. Wei, Z. Kang, L. Hu, and C. Li, "Fast color balance and multi-path fusion for sandstorm image enhancement," *Signal, Image and Video Processing*, vol. 15, no. 3, pp. 637–644, 2021.

- [61] G. Gao, H. Lai, Y. Liu, L. Wang, and Z. Jia, "Sandstorm image enhancement based on YUV space," *Optik*, vol. 226, p. 165659, 2021.
- [62] Y. Si, F. Yang, Y. Guo, W. Zhang, and Y. Yang, "A comprehensive benchmark analysis for sand dust image reconstruction," *Journal of Visual Communication and Image Representation*, vol. 89, p. 103638, 2022.
- [63] X. Dong, Y. Pang, and J. Wen, "Fast efficient algorithm for enhancement of low lighting video," in *ACM SIGGRAPH 2010 Posters*, 2010, pp. 1–1.
- [64] X. Jiang, H. Yao, S. Zhang, X. Lu, and W. Zeng, "Night video enhancement using improved dark channel prior," in *IEEE International Conference on Image Processing*. IEEE, 2013, pp. 553–557.
- [65] E. D. Pisano, S. Zong, B. M. Hemminger, M. DeLuca, R. E. Johnston, K. Muller, M. P. Braeuning, and S. M. Pizer, "Contrast limited adaptive histogram equalization image processing to improve the detection of simulated spiculations in dense mammograms," *Journal of Digital imaging*, vol. 11, no. 4, pp. 193–200, 1998.
- [66] E. H. Land, "The retinex theory of color vision," *Scientific american*, vol. 237, no. 6, pp. 108–129, 1977.
- [67] S. Wang, J. Zheng, H.-M. Hu, and B. Li, "Naturalness preserved enhancement algorithm for non-uniform illumination images," *IEEE transactions on image processing*, vol. 22, no. 9, pp. 3538–3548, 2013.
- [68] X. Guo, Y. Li, and H. Ling, "Lime: Low-light image enhancement via illumination map estimation," *IEEE Transaction on Image Processing*, vol. 26, no. 2, pp. 982–993, Feb. 2016.
- [69] C. Guo, C. Li, J. Guo, C. C. Loy, J. Hou, S. Kwong, and R. Cong, "Zero-reference deep curve estimation for low-light image enhancement," in *Proceedings of the IEEE/CVF Conference on Computer Vision and Pattern Recognition*, 2020, pp. 1780–1789.
- [70] Y. Wang, R. Wan, W. Yang, H. Li, L.-P. Chau, and A. Kot, "Low-light image enhancement with normalizing flow," in *Proceedings of the AAAI Conference on Artificial Intelligence*, vol. 36, no. 3, 2022, pp. 2604–2612.
- [71] J. Liu, D. Xu, W. Yang, M. Fan, and H. Huang, "Benchmarking low-light image enhancement and beyond," *International Journal of Computer Vision*, vol. 129, no. 4, pp. 1153–1184, 2021.
- [72] C. O. Ancuti, C. Ancuti, R. Timofte, and C. D. Vleeschouwer, "I-HAZE: a dehazing benchmark with real hazy and haze-free indoor images," in *International Conference on Advanced Concepts for Intelligent Vision Systems*, 2018, pp. 620–631.
- [73] ——, "O-HAZE: A dehazing benchmark with real hazy and haze-free outdoor images," in *Proceedings of the IEEE Conference on Computer Vision and Pattern Recognition Workshops (CVPRW)*, 2018, pp. 867–875.
- [74] C. O. Ancuti, C. Ancuti, M. Sbert, and R. Timofte, "Dense Haze: A benchmark for image dehazing with dense-haze and haze-free images," in *IEEE International Conference on Image Processing (ICIP)*, 2019, pp. 1014–1018.
- [75] C. Ancuti, C. O. Ancuti, and R. Timofte, "NTIRE 2018 challenge on image dehazing: Methods and results," in *Proceedings of the IEEE Conference on Computer Vision and Pattern Recognition Workshops (CVPRW)*, 2018, pp. 891–901.
- [76] C. O. Ancuti, C. Ancuti, R. Timofte, L. V. Gool, L. Zhang, and M.-H. Yang, "NTIRE 2019 image dehazing challenge report," in *Proceedings of the IEEE Conference on Computer Vision and Pattern Recognition Workshops (CVPRW)*, 2019, pp. 2241–2253.
- [77] H. Ji, W. Yu, and Y. Li, "A rank revealing randomized singular value decomposition (R3SVD) algorithm for low-rank matrix approximations," *arXiv preprint arXiv:1605.08134*, 2016.
- [78] S. Boyd, N. Parikh, E. Chu, B. Peleato, and J. Eckstein, *Distributed Optimization and Statistical Learning via the Alternating Direction Method of Multipliers*. Now Publishers Inc, 2011.
- [79] D. Berman, T. Treibitz, and S. Avidan, "Air-light estimation using haze-lines," in *2017 IEEE International Conference on Computational Photography (ICCP)*, 2017, pp. 1–9.
- [80] Y. Zhu, G. Tang, X. Zhang, J. Jiang, and Q. Tian, "Haze removal method for natural restoration of images with sky," *Neurocomputing*, vol. 275, pp. 499–510, 2018.
- [81] S. Zhang, C. Qing, X. Xu, J. Jin, and H. Qin, "Dehazing with improved heterogeneous atmosphere light estimation and a non-linear color attenuation prior model," in *2016 10th International Symposium on Communication Systems, Networks and Digital Signal Processing (CSNDSP)*. IEEE, 2016, pp. 1–6.
- [82] X. Qin, Z. Wang, Y. Bai, X. Xie, and H. Jia, "Ffa-net: Feature fusion attention network for single image dehazing," in *Proceedings of the AAAI Conference on Artificial Intelligence*, vol. 34, no. 07, 2020, pp. 11 908–11 915.
- [83] D. Chen, M. He, Q. Fan, J. Liao, L. Zhang, D. Hou, L. Yuan, and G. Hua, "Gated context aggregation network for image dehazing and deraining," in *IEEE Winter Conference on Applications of Computer Vision (WACV)*. IEEE, 2019, pp. 1375–1383.
- [84] X. Liu, Y. Ma, Z. Shi, and J. Chen, "Griddehazenet: Attention-based multi-scale network for image dehazing," in *Proceedings of the IEEE International Conference on Computer Vision*, 2019, pp. 7314–7323.
- [85] B. Li, W. Ren, D. Fu, D. Tao, D. Feng, W. Zeng, and Z. Wang, "Benchmarking single-image dehazing and beyond," *IEEE Transactions on Image Processing*, vol. 28, no. 1, pp. 492–505, 2018.
- [86] X. Zhang, H. Dong, J. Pan, C. Zhu, Y. Tai, C. Wang, J. Li, F. Huang, and F. Wang, "Learning to restore hazy video: A new real-world dataset and a new method," in *Proceedings of the IEEE Conference on Computer Vision and Pattern Recognition (CVPR)*, 2021, pp. 9239–9248.
- [87] J. Pan, D. Sun, H. Pfister, and M.-H. Yang, "Deblurring images via dark channel prior," *IEEE Transactions on Pattern Analysis and Machine Intelligence*, vol. 40, no. 10, pp. 2315–2328, 2018.
- [88] C. Chen, M. N. Do, and J. Wang, "Robust image and video dehazing with visual artifact suppression via gradient residual minimization," in *Proceedings of the European Conference on Computer Vision (ECCV)*. Springer, 2016, pp. 576–591.
- [89] C.-Y. Li, J.-C. Guo, R.-M. Cong, Y.-W. Pang, and B. Wang, "Underwater image enhancement by dehazing with minimum information loss and histogram distribution prior," *IEEE Transactions on Image Processing*, vol. 25, no. 12, pp. 5664–5677, 2016.
- [90] Y.-T. Peng and P. C. Cosman, "Underwater image restoration based on image blurriness and light absorption," *IEEE Transactions on Image Processing*, vol. 26, no. 4, pp. 1579–1594, 2017.
- [91] X. Fu, D. Zeng, Y. Huang, X.-P. Zhang, and X. Ding, "A weighted variational model for simultaneous reflectance and illumination estimation," in *Proceedings of the IEEE Conference on Computer Vision and Pattern Recognition (CVPR)*, 2016, pp. 2782–2790.
- [92] L. Ma, D. Jin, R. Liu, X. Fan, and Z. Luo, "Joint over and under exposures correction by aggregated retinex propagation for image enhancement," *IEEE Signal Processing Letters*, vol. 27, pp. 1210–1214, 2020.
- [93] M. Li, J. Liu, W. Yang, X. Sun, and Z. Guo, "Structure-revealing low-light image enhancement via robust Retinex model," *IEEE Transactions on Image Processing*, vol. 27, no. 6, pp. 2828–2841, 2018.
- [94] R. Wang, X. Xu, C.-W. Fu, J. Lu, B. Yu, and J. Jia, "Seeing dynamic scene in the dark: A high-quality video dataset with mechatronic alignment," in *Proceedings of the IEEE International Conference on Computer Vision (ICCV)*, 2021, pp. 9700–9709.
- [95] R. Wang, Q. Zhang, C.-W. Fu, X. Shen, W.-S. Zheng, and J. Jia, "Underexposed photo enhancement using deep illumination estimation," in *Proceedings of the IEEE Conference on Computer Vision and Pattern Recognition (CVPR)*, 2019, pp. 6849–6857.
- [96] A. Galdran, A. Alvarez-Gila, A. Bria, J. Vazquez-Corral, and M. Bertalmio, "On the duality between retinex and image dehazing," in *Proceedings of the IEEE Conference on Computer Vision and Pattern Recognition (CVPR)*, 2018, pp. 8212–8221.
- [97] K. He, J. Sun, and X. Tang, "Single image haze removal using dark channel prior," in *Proceedings of the IEEE Conference on Computer Vision and Pattern Recognition (CVPR)*, 2009, pp. 1956–1963.
- [98] R. E. Lukac, *Single-sensor imaging: methods and applications for digital cameras (1st ed.)*. CRC Press, 2018.
- [99] Q. Yan, L. Xu, and J. Jia, "Dense scattering layer removal," in *SIGGRAPH Asia Technical Briefs*, 2013, pp. 1–4.
- [100] Z. Yue, H. Yong, Q. Zhao, D. Meng, and L. Zhang, "Variational denoising network: Toward blind noise modeling and removal," *Advances in Neural Information Processing Systems*, vol. 32, pp. 1690–1701, 2019.
- [101] X. Shen, Q. Yan, L. Xu, L. Ma, and J. Jia, "Multispectral joint image restoration via optimizing a scale map," *IEEE Transactions on Pattern Analysis and Machine Intelligence*, vol. 37, no. 12, pp. 2518–2530, 2015.
- [102] B. Garcia-Garcia, T. Bouwmans, and A. J. R. Silva, "Background subtraction in real applications: Challenges, current models and future directions," *Computer Science Review*, vol. 35, p. 100204, 2020.



**Jun Liu** is currently an associate professor in the School of Mathematics and Statistics, Northeast Normal University. He received the Ph.D. degree from the University of Electronic Science and Technology of China, Chengdu, Sichuan, China, in 2015. He was a visiting student with the Department of Mathematics, University of California, Los Angeles. His research interests include the scientific computation and variational methods in mathematical modeling of image processing and computer vision.



**Ryan Wen Liu** received the B.S. degree (Hons.) in Information and Computing Science from the Wuhan University of Technology, Wuhan, China, in 2009, and the Ph.D. degree from The Chinese University of Hong Kong, Hong Kong, in 2015. He is currently an Associate Professor with the School of Navigation, Wuhan University of Technology, Wuhan, China. His research interests mainly include computer vision, trajectory data mining, and multi-source information fusion. He is an Associate Editor of *International Journal on Semantic Web and Information Systems*.



machine learning.

**Jianing Sun** received his B.S. degree, M.S. degree and Ph. degree in computational mathematics from the School of Mathematics, Jilin University, Jilin Province, China in 2000, 2003 and 2008, respectively. Currently, he is an associate professor in the School of Mathematics and Statistics, Northeast Normal University. He is also invited by the National Center for Applied Mathematics in Jilin to serve as a scientific consultant. His research interests include computer vision, computational photography, big data and



**Tieyong Zeng** is currently a Professor in the Department of Mathematics, The Chinese University of Hong Kong. He received the B.S. degree from Peking University, Beijing, China, M.S. degree from Ecole Polytechnique, Palaiseau, France, and Ph.D. degree from the University of Paris XIII, Paris, France, in 2000, 2004, and 2007, respectively. In 2007-2008, he was a Post-Doctoral Researcher with the Centre de Mathématiques et de Leurs Applications, ENS de Cachan, Cachan, France. In 2008-2018, he was an Assistant and then Associate Professor in the Department of Mathematics, Hong Kong Baptist University, Kowloon Tong, Hong Kong. His research interests are image processing, statistical/machine learning, and scientific computing.